Vortex structure of thin mesoscopic disks with enhanced surface superconductivity

S. V. Yampolskii* and F. M. Peeters†
Departement Natuurkunde, Universiteit Antwerpen (UIA), Universiteitsplein 1, B-2610 Antwerpen, Belgium
(Received 14 December 1999; revised manuscript received 15 June 2000)

The vortex state in a thin mesoscopic disk surrounded by a medium which enhances surface superconductivity is investigated theoretically in the framework of the phenomenological Ginzburg-Landau theory. We calculated the dependences of both the ground and metastable states on an external magnetic field perpendicular to the disk plane for different values of the order parameter angular moment, i.e., the vorticity. The magnetic field-temperature phase diagram is obtained and the regions of existence of the multivortex state and the giant vortex state are found. We analyzed the phase transitions between these states. Our results are also applicable for the analysis of the vortex state in extreme type-II mesoscopic disks.

I. INTRODUCTION

The progress of nanofabrication technologies during the last years resulted in an increase of interest in the study of superconducting properties of mesoscopic samples. A mesoscopic sample is such that its size is comparable to the coherence length (ξ) and the magnetic-field penetration length (λ). Mesoscopic disks have been one of the most popular study objects[1–11] in this respect. The behavior of such structures in an external magnetic field (H) is strongly influenced by the sample shape[12] and may lead to various superconducting states and different phase transitions between them. Jumps in magnetization were observed when varying an applied magnetic field or temperature (T).[2]

Theoretical studies have shown that in mesoscopic disks surrounded by vacuum or an insulator medium two kinds of superconducting states can exist. First, there is a circular symmetric state with a fixed value of the angular momentum (or the giant vortex). The observed magnetization jumps correspond to first-order phase transitions between the giant vortices with different angular momentum.[3,5] Second, in disks with a sufficiently large radius multivortex structures can exist which are the analogue of the Abrikosov flux-line lattice in a bulk superconductor. These states can be represented as a mixture of giant vortex ones with different angular momentum. For multivortex states it is also possible to introduce an effective total angular momentum, which is nothing else than the number of vortices in the disk, i.e., the vorticity. With changing the magnetic field there is a second-order phase transition between the multivortex and the giant vortex state.[6]

The size of the superconducting sample may strongly influence the magnetic field at which the superconductor to normal-state transition takes place. In an infinite cylinder, surface superconductivity exists up to the surface superconducting critical magnetic field $H_{c3}=1.69H_{c2}$, but in mesoscopic samples the nucleation field increases with the decrease of the sample size.[4,5,12–15]

The nucleation field and the critical temperature can also be influenced by changing the conditions at the sample surface. Usually, the contact of a superconductor with a normal metal (the proximity effect) is mentioned in this respect (see, for example, Ref. 16). This effect suppresses superconductivity and decreases both critical parameters. It was shown that for a thin type-II superconducting cylinder it leads to a minimum cylinder radius below which superconductivity can no longer exist.[17] It is known that the opposite, namely enhancement of surface superconductivity, is also possible. In particular, it was found that a bulk superconductor after *cold working* of the sample surface revealed a surface region of enhanced transition temperature.[18] For such a superconductor the nucleation field was larger than those expected from a uniform sample. Also both critical parameters (the critical temperature and the nucleation field) can be increased by the twinning planes inside a bulk sample (see, for example, Ref. 19). There have been two other possibilities for enhancement of superconductivity at the sample surface been described in the literature,[20] which are due to contacting the superconductor with a suitably chosen medium. One possibility is to choose for the contacted layer a material which has a higher transition temperature in the bulk than the superconductor under study. With other words, this is an enhancement of superconductivity caused by the proximity effect. Another way of obtaining a surface with enhanced superconductivity is by making a contact between the superconductor and a semiconductor, such that there is suitable overlap of the band gap of the semiconductor with the superconducting gap.

It was shown previously that the physics involved in contacts of a superconductor with a medium which enhances the superconducting properties of the surface are analogous to the wetting problem of a fluid in contact with a surface and that the superconductor–normal-state phase diagram becomes substantially richer. For type-I bulk superconductors it leads to a surface phase transition in which the superconductor/vacuum interface delocalizes from the sample surface into the interior.[21] These interface delocalization transitions are analogous to wetting transitions in adsorbed fluids. Further, using ideas from wetting theory, the shape of a superconducting ''drop'' near the sample surface was calculated.[22] Here we will investigate how this enhancement of superconductivity at the boundary influences the superconducting state in mesoscopic disks.

In the present paper we investigated the influence of surface enhancement of superconductivity on the vortex structure of a thin mesoscopic disk. We use the phenomenological

Ginzburg-Landau (GL) theory. Although this theory has only a firm mathematical derivation in a narrow range of both temperature and magnetic field close to the superconducting–normal-state phase boundary[16] it turns out that it gives also very good results inside the superconducting phase diagram. In particular, it was used successfully to describe mesoscopic samples in the whole H-T region.[3–11,14,23]

The paper is organized as follows. In Sec. II we present our theoretical model and indicate how the influence of the boundary is included through a specific boundary condition. In Sec. III we discuss the giant vortex states. The stability of multivortex states and transitions between them are investigated in Sec. IV. In Sec. V we give the H-T phase diagram for thin disks and investigate the influence of superconductivity enhancement resulting from the specific boundary conditions at top and bottom surface of the disk as compare to those at the disk radial boundary. Our results are summarized in Sec. VI.

II. THEORETICAL MODEL

We consider a mesoscopic superconducting disk with radius R and thickness d surrounded by a medium which enhances superconductivity at the sample surface. The external magnetic field $\vec{H}=(0,0,H)$ is uniform and directed normal to the disk plane. We have to solve the system of two coupled nonlinear GL equations which determine the distribution of both the superconducting order parameter, $\Psi(\vec{r})$, and the magnetic field [or vector potential $\vec{A}(\vec{r})$] inside and outside the superconductor,

$$\frac{1}{2m}\left(-i\hbar\vec{\nabla}-\frac{2e\vec{A}}{c}\right)^2\Psi=-\alpha\Psi-\beta\Psi|\Psi|^2, \tag{1}$$

$$\vec{\nabla}\times\vec{\nabla}\times\vec{A}=\frac{4\pi}{c}\vec{j}, \tag{2}$$

where the density of the superconducting current $\vec{j}$ is given by

$$\vec{j}=\frac{e\hbar}{im}(\Psi^*\vec{\nabla}\Psi-\Psi\vec{\nabla}\Psi^*)-\frac{4e^2}{mc}|\Psi|^2\vec{A}. \tag{3}$$

Here $\vec{r}=(\vec{\rho},z)$ is the three-dimensional position in space. Due to the circular symmetry of the disk we use cylindrical coordinates: ρ is the radial distance from the disk center, φ is the azimuthal angle and the z axis is taken perpendicular to the disk plane, where the disk lies between $z=-d/2$ and $z=d/2$.

Equations (1)–(3) have to be supplemented by boundary conditions (BC) for $\Psi(\vec{r})$ and $\vec{A}(\vec{r})$. The condition for the superconducting condensate on the sample surface can in general be written as[16,21,22,24]

$$\vec{n}\cdot\left(-i\hbar\vec{\nabla}-\frac{2e\vec{A}}{c}\right)\Psi\Big|_S=\frac{i}{b}\Psi\Big|_S, \tag{4}$$

where $\vec{n}$ is the unit vector normal to the disk surface and b is a surface extrapolation length which is the effective penetration depth of the order parameter into the surrounding medium.[16] For both the superconductor-vacuum and the superconductor-insulator boundary one has $b\to\infty$. The case $b<0$ corresponds to surface enhancement of superconductivity. The opposite case $b>0$ corresponds to surface suppression of the superconducting order parameter. The boundary condition for the vector potential has to be taken far away from the disk where the magnetic field becomes equal to the external applied field H

$$\vec{A}|_{r\to\infty}=\frac{1}{2}H\rho\vec{e}_\varphi, \tag{5}$$

where $\vec{e}_\varphi$ denotes the azimuthal direction.

Using dimensionless variables and the London gauge $\mathrm{div}\,\vec{A}=0$ we can rewrite the system of Eqs. (1)–(3) and BC (4) in the following form:

$$(-i\vec{\nabla}-\vec{A})^2\psi=\psi-\psi|\psi|^2, \tag{6}$$

$$-\kappa^2\Delta\vec{A}=\frac{1}{2i}(\psi^*\vec{\nabla}\psi-\psi\vec{\nabla}\psi^*)-|\psi|^2\vec{A}, \tag{7}$$

$$\vec{n}\cdot(-i\vec{\nabla}-\vec{A})\psi\Big|_S=\frac{i}{b}\psi\Big|_S. \tag{8}$$

Here all distances are measured in units of the coherence length $\xi=\hbar/\sqrt{2m|\alpha|}$, the order parameter in $\Psi_0=\sqrt{|\alpha|/\beta}$, the vector potential in $c\hbar/2e\xi$, $\kappa=\lambda/\xi$ is the GL parameter, and $\lambda=c\sqrt{m/\pi}/4e\Psi_0$ is the London penetration depth. We measure the magnetic field in $H_{c2}=c\hbar/2e\xi^2=\kappa\sqrt{2}H_c$, where $H_c=\sqrt{4\pi\alpha^2/\beta}$ is the thermodynamical critical field.

The free energy of the superconducting state, measured in $F_0=H_c^2V/8\pi$ units, is determined by the expression

$$F=\frac{2}{V}\Bigg[\int dV\Big(-|\psi|^2+\frac{1}{2}|\psi|^4+|-i\vec{\nabla}\psi-\vec{A}\psi|^2+\kappa^2[\vec{h}(\vec{r})-\vec{H}]^2\Big)+\frac{1}{b}\oint dS|\psi|^2\Bigg], \tag{9}$$

$$\vec{h}(\vec{r})=\vec{\nabla}\times\vec{A}(\vec{r}).$$

The last term in Eq. (9) is the surface contribution which is due to the boundary condition (8) and it provides continuity of the normal component of the superconducting current. One can see that in the $b<0$ case this term reduces the free energy.

We restrict ourselves to sufficiently thin disks such that $d\ll\xi,\lambda$. In this case, to a first approximation, the magnetic field is uniform inside the disk and equal to the external one, i.e., we are allowed to neglect the contribution of the supercurrents to the magnetic field. Within this approximation we have to solve only the first GL Eq. (6) with $\vec{A}=\vec{A}_0=(0,H\rho/2,0)$.

First, we determine the z dependence of $\psi(\vec{r})$. Expanding it in a Fourier series $\psi(\vec{r})=\Sigma_k\psi_k(\vec{\rho})\exp(ikz)$ and using the same BC (8) on the top ($z=d/2$) and bottom ($z=-d/2$) of the disk surface we obtain a nonlinear equation for each k:

$$\frac{\exp(ikd)+1}{\exp(ikd)-1}=ikb. \tag{10}$$

In the $d\to 0$ limit the lowest k solution gives

$$k^2=-\frac{2}{bd}. \tag{11}$$

After substituting $k\to ik$ we have $\psi=\psi(\vec{\rho})\cosh kz$ (where now k is real: $k=\sqrt{-2/bd}$). Because $-d/2<z<d/2$ we have $-\sqrt{-2d/b}<kz<\sqrt{-2d/b}$ and consequently, for $|d/b|\ll 1$, $\psi(\vec{r})$ varies very slowly along the z direction. Therefore we are allowed to average the order parameter $\psi(\vec{r})$ over the disk thickness as it was done in Ref. 5 (this averaging corresponds also to the thin-film limit of the results of Ref. 25):

$$\langle\psi(\vec{r})\rangle=\frac{1}{d}\int_{-d/2}^{d/2}\psi(\vec{\rho})\cosh kz\,dz$$

$$=\psi(\vec{\rho})\cdot\frac{\sinh kd/2}{kd/2}\underset{d\to 0}{\to}\psi(\vec{\rho}). \tag{12}$$

The same averaging of Eq. (6) yields for $\psi(\vec{\rho})$

$$\langle(-i\vec{\nabla}-\vec{A})^2\rangle\psi(\vec{\rho})=\left[-\frac{1}{\rho}\frac{\partial}{\partial\rho}\rho\frac{\partial}{\partial\rho}-\frac{1}{\rho^2}\frac{\partial^2}{\partial\varphi^2}+iH\frac{\partial}{\partial\varphi}+\left(\frac{H\rho}{2}\right)^2-k^2\right]\psi(\vec{\rho})$$

$$=\psi(\vec{\rho})-\psi(\vec{\rho})|\psi(\vec{\rho})|^2, \tag{13}$$

with the boundary condition

$$\left.\frac{\partial\psi(\vec{\rho})}{\partial\rho}\right|_{\rho=R}=-\frac{1}{b}\psi(\vec{\rho})\Big|_{\rho=R}. \tag{14}$$

After this averaging the problem for $\psi(\vec{r})$ is reduced to a two-dimensional one for $\psi(\vec{\rho})$ like in Refs. 5 and 6. But in contrast to Refs. 5 and 6 there is still a dependence on the disk thickness which is determined by the parameter k in Eq. (13). Notice also that the boundary condition (14) introduces a dependence on the phenomenological parameter b. It determines the value of the derivative of ψ at the surface. It is obvious that for $b<0$ we have a positive derivative $\partial\psi(\vec{\rho})/\partial\rho$ at the surface, i.e., surface enhancement of superconductivity.

III. GIANT VORTEX STATES

The giant vortex state has cylindrical symmetry and consequently the order parameter can be written as $\psi(\vec{\rho})=f(\rho)\exp(iL\varphi)$. The stable states are obtained in the following way. From the *linearized* GL Eq. (13) with the BC (14) we find $f(\rho)$ up to a multiplying constant. This function is then inserted into the free-energy expression (9) which after minimization determines the constant in $f(\rho)$ and the energy value corresponding to the stable state. It can be shown that the present approach and the one of Ref. 5, which was based on a solution of the nonlinear GL Eq. (13), result into the same functional $F(H)$ dependence in case of giant vortex states.

The linearized GL equation for $f(\rho)$ takes the form

$$\hat{L}f=0,\quad \hat{L}=-\frac{1}{\rho}\frac{\partial}{\partial\rho}\rho\frac{\partial}{\partial\rho}+\left(\frac{L}{\rho}-\frac{H\rho}{2}\right)^2-1-k^2. \tag{15}$$

The $\hat{L}$ operator differs by the last constant term from the one studied previously.[5,26] The superconducting state corresponds to the negative eigenvalues of the $\hat{L}$ operator. The nucleation field H_{nuc} for the giant vortex state with fixed L is reached when the minimal eigenvalue of the $\hat{L}$ operator for the same angular momentum becomes equal to zero.

The eigenvalues and eigenfunctions of the $\hat{L}$ operator are found from the equation

$$\hat{L}f_{L,n}(\rho)=\Lambda f_{L,n}(\rho), \tag{16}$$

where $f_{L,n}(\rho)$ satisfies $\rho(\partial f/\partial\rho)|_{\rho=0}=0$ at the disk center. The index $n=1,2,\ldots$ enumerates the different states for the same R and L values. The eigenfunctions of Eq. (16) are

$$f_{L,n}(\rho)=\left(\frac{H\rho^2}{2}\right)^{L/2}\exp\left(-\frac{H\rho^2}{4}\right)M\left(-\nu_n,L+1,\frac{H\rho^2}{2}\right), \tag{17}$$

where $M(a,c,y)$ is the Kummer function.[27] The BC (14) results into a nonlinear equation for ν_n,

$$\left(L-\frac{\Phi}{2}+\frac{R}{b}\right)M\left(-\nu_n,L+1,\frac{\Phi}{2}\right)-\frac{\nu_n\Phi}{L+1}\times M\left(-\nu_n+1,L+2,\frac{\Phi}{2}\right)=0, \tag{18}$$

where $\Phi=HR^2$ is the magnetic flux through the disk in the absence of any flux expulsion. The eigenvalues of $\hat{L}$ are

$$\Lambda=H(1+2\nu_n)-1-k^2. \tag{19}$$

The magnetic-field dependences of Λ for the lowest angular momenta L are shown in Figs. 1(a)–(c) for three different b values. All numerical calculations were done for a disk thickness $d/\xi=0.1$ which is within the thin disk approximation. The negative L values (dotted curves in Fig. 1) correspond to vortices with flux Φ directed opposite to the appied magnetic field (they are the analog to ''antivortices'' in conventional superconductors). The dashed curve in Fig. 1(c) is for the first radial excited state, i.e., $L=0$ and $n=1$. The dotted horizontal line corresponds to the $\Lambda=0$ level. In Fig. 2 the radial dependence of the superconducting density $|\psi|^2$ is shown for all the possible L values at $H=H_{c2}$ in case of $\xi/b=-0.2$. The same curve conventions are used as in Fig. 1. Notice that for the excited state $L=0$, $n=1$ (dashed curve in Fig. 2) the order parameter vanishes inside the disk (at $\rho=1.25\xi$) and a ringlike vortex is formed.[28] From Fig. 1 one can see that with increasing $|\xi/b|$: (i) the eigenvalues Λ become more negative; (ii) the magnetic-field range over which solutions of Eq. (18) can be found increases; and (iii) the number of possible solutions increases substantially.

The eigenvalues Λ determine the minimal free energy F of the giant vortices. For the giant vortex state we consider

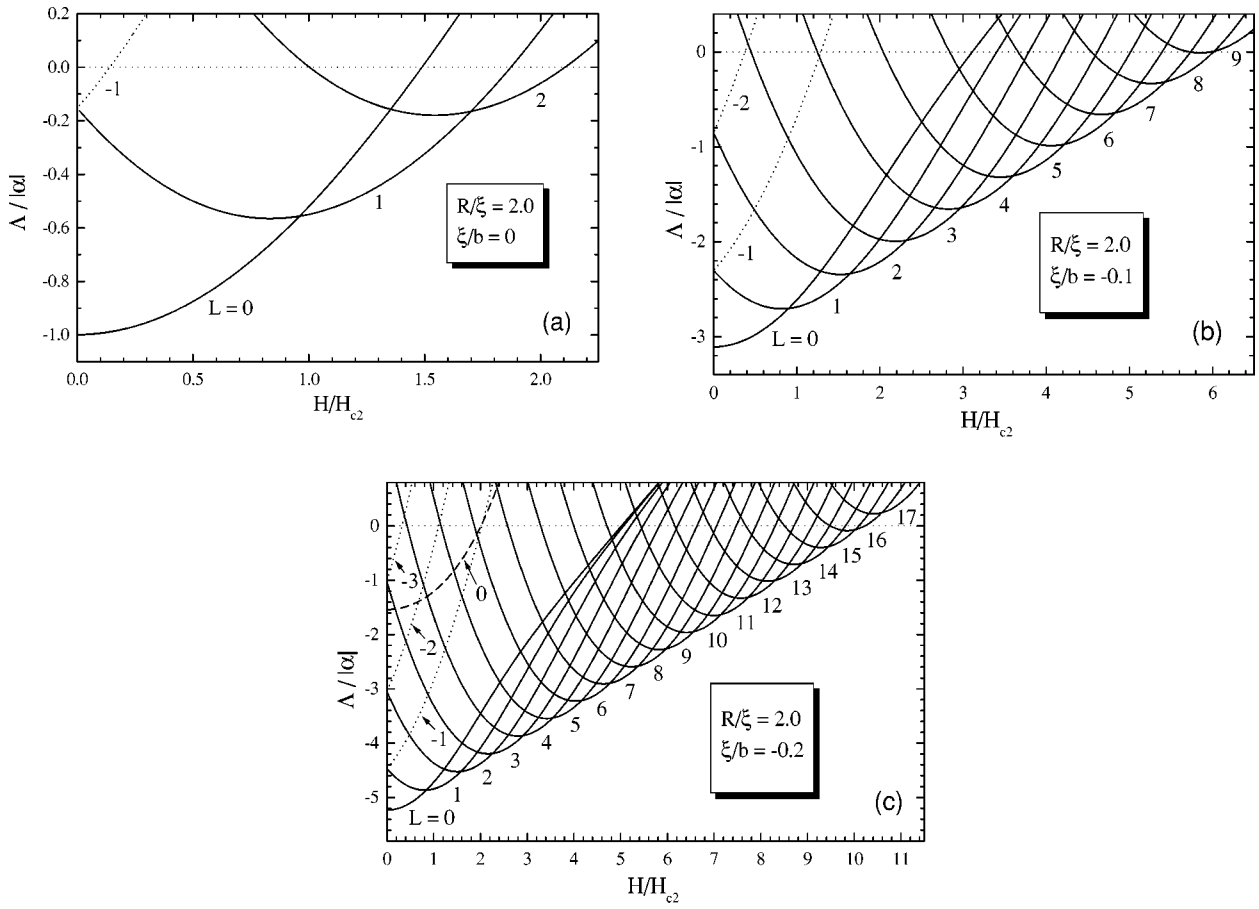

FIG. 1. The magnetic-field dependence of the lowest eigenvalues of the linearized first GL equation for different angular momenta L and for (a) $\xi/b=0$, (b) $\xi/b=-0.1$, and (c) $\xi/b=-0.2$.

only states which lie below the $F=0$ level. In this approximation the order parameter and minimal energy value are

$$\psi(\vec{\rho})=\left(-\Lambda\frac{I_2}{I_1}\right)^{1/2} f_{L,n}(\rho)\exp(iL\varphi) \tag{20}$$

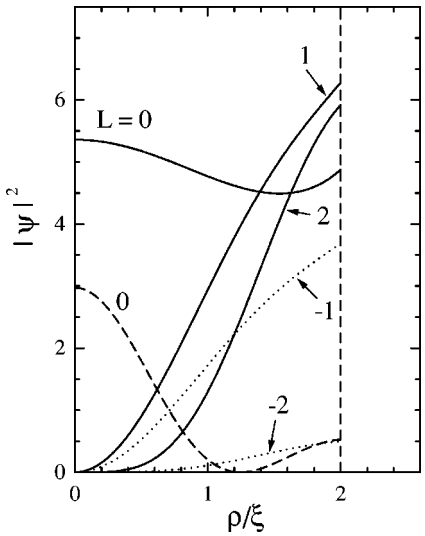

FIG. 2. The Cooper pair density for the giant vortex states with angular momenta $L=0,1,2$ (solid curves), the antivortex states $L=-1,-2$ (dotted curves) and the ring vortex state $L=0, n=1$ (dashed curve) at the magnetic field $H=H_{c2}$ for $R/\xi=2.0$, $\xi/b=-0.2$.

and

$$F=-\Lambda^2\frac{2\pi d}{V}\frac{I_2^2}{I_1}, \tag{21}$$

respectively, where

$$I_1=\int_0^R \rho d\rho\, f_{L,n}^4(\rho), \quad I_2=\int_0^R \rho d\rho\, f_{L,n}^2(\rho).$$

The dependence of F on the magnetic field H are shown in Fig. 3 for the same angular momenta L shown in Fig. 1, with the exception of Fig. 3(c) where the $F(H)$ curves with $L>11$ are not plotted. The highest value of vorticity in this disk is $L=16$ [see Fig. 1(c)]. The dotted horizontal line in Fig. 3 (and in the following figures) corresponds to the zero energy level. From a comparison of the magnetic-field dependence of $F(H)$ for $\xi/b=0$ and the one with $\xi/b\neq 0$ we clearly observe an enhancement of superconductivity (with increase of $|\xi/b|$) and the number of possible giant vortex states increases. Also a significant increase of the surface nucleation field H_{nuc} is found. The envelope of the lowest parts of the curves in Fig. 3 represents the field dependence of the ground-state energy.

In Fig. 4 the ground-state energies are shown for different values of ξ/b. Notice that the enhancement of superconductivity at the surface leads to a decrease of the energy of the ground state. With increasing applied field the $L\rightarrow L+1$ phase transitions take place at the field where the corre-

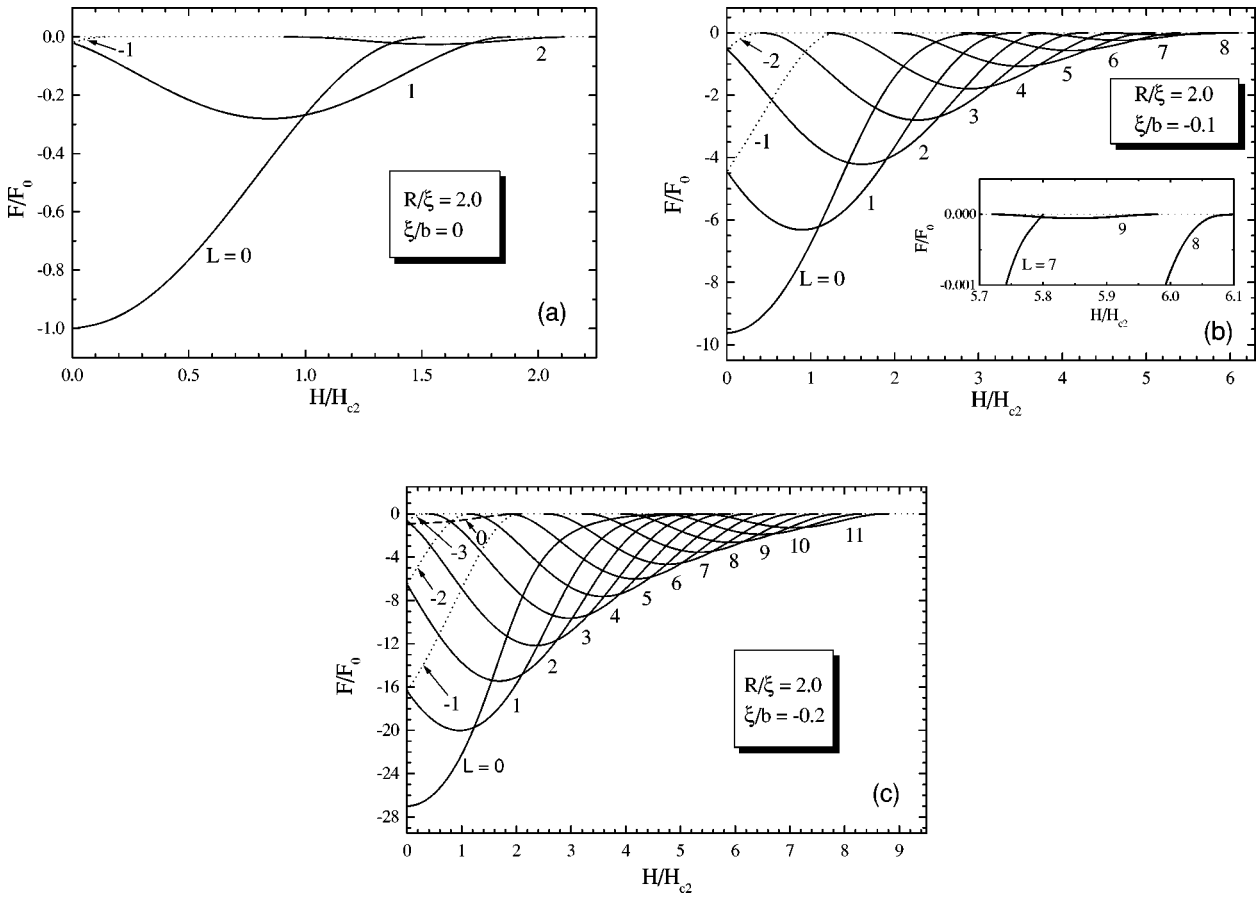

FIG. 3. The free energy of the giant vortex states with different angular momenta L as a function of the external magnetic field for (a) $\xi/b=0$, (b) $\xi/b=-0.1$, and (c) $\xi/b=-0.2$. For the last case only the states with $L\leqslant 11$ are shown. The maximal vorticity value is $L=16$ in this case [see Fig. 1(c)].

sponding curves cross (for example, the $0\rightarrow 1$ transition occurs at $H=1.098H_{c2}$ for $\xi/b=-0.1$). The crossing points are practically independent of the value of ξ/b. In the inset of Fig. 4 the $|\psi(r)|^2$ dependence is shown for $\xi/b=-0.2$ at fields corresponding to the $L=0$ and $L=1$ ground states ($H=0.5H_{c2}$ and $H=1.5H_{c2}$, respectively). The $L\rightarrow L+1$ transitions are of first order and lead to jumps in the magnetization $M=-(\partial F/\partial H)$. The corresponding $M(H)$ curves are shown in Fig. 5. The phase transition from the superconducting to the normal state is of second order [all curves $F(H)$ reach the $F=0$ line with zero derivative]. The curves $F(H)$ in Fig. 3 which are situated above the ground-state energy correspond to metastable giant vortex states. With

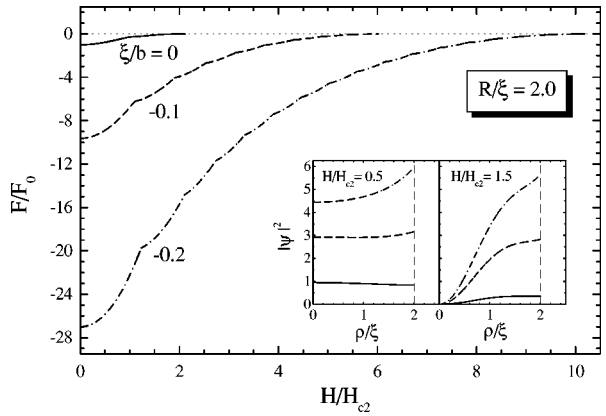

FIG. 4. The ground-state energy of the giant vortex state for different values of the ξ/b parameter. The inset depicts the radial Cooper pair density for two magnetic fields, corresponding to the $L=0$ and $L=1$ state, where the same curve conventions are used as in the main figure.

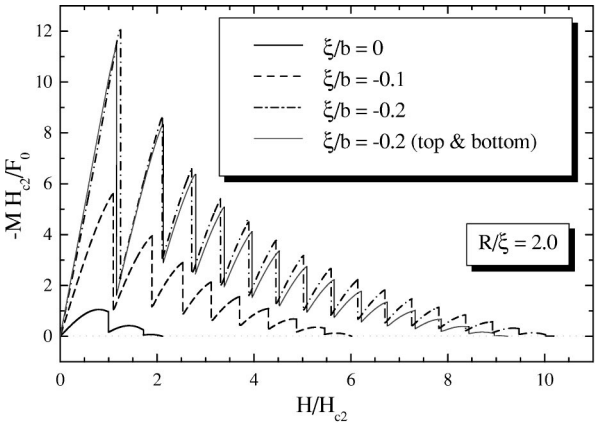

FIG. 5. The magnetic-field dependence of the disk magnetization for the ground giant vortex state corresponding to the states of Fig. 4. For comparison with the calculations from Sec. V the magnetization of a disk with enhancement of superconductivity only on the top and bottom surfaces is shown by the thin solid curve for the case $\xi/b=-0.2$.

increasing applied field the transition from the Meissner state ($L=0$) to the normal state goes through a set of consecutive first-order transitions between the L and $L+1$ giant vortices which is finished by a second-order transition to the normal state. Notice that in the $\xi/b=-0.1$ case [inset in Fig. 3(b)] a metastable state with $L=9$ occurs which does not become a ground state. This state is separated from the $L=8$ state because the crossing point of the corresponding eigenvalue curves of Fig. 1(b) lies *higher* than the $\Lambda=0$ level. With increasing $|\xi/b|$ value this crossing point moves below the $\Lambda=0$ level and a transition from the $L=8$ state to the $L=9$ state becomes possible.

The free energy is strongly influenced by the enhancement of superconductivity at the disk surface. The boundary condition (4): (i) gives b terms which leads to a k^2 shift in the energy Λ towards lower energy [Eq. (19)] due to the boundary condition on the top and bottom of the disk, and (ii) modifies the equation for the boundary condition (18) giving ν_n a b dependence which is due to the radial boundary condition, i.e., the side boundary of the disk.

IV. MULTIVORTEX STATES

For sufficiently large disks the giant vortex state can break up into multivortices.[6–8] In order to investigate such structures in our case we use the method proposed by Schweigert *et al.*[6] and Palacios[7,8] and extend it here to determine also the stability of the different multivortex configurations. Following Refs. 7 and 23 the order parameter of the multivortex state is written as a linear combination of the eigenfunctions of the linearized GL Eq. (15),

$$\psi(\vec{\rho})=\sum_{L_j=0}^{L}\sum_{n} C_{L_j,n} f_{L_j,n}(\rho)\exp(iL_j\varphi), \tag{22}$$

where L is now the value of the effective total angular momentum which is equal to the number of vortices in the disk, and n enumerates the different radial states for the same L_j. We restricted ourselves to the lowest state eigenfunctions and took only $n=0$. The index n will therefore be omitted from now on.

Substituting Eq. (22) in the free-energy expression (9) we obtain F as a function of the complex parameters $\{C_{L_j}\}$. Minimization of F with respect to these parameters allows us to find the equilibrium vortex configurations and to determine their stability. The extremal points are determined by the solutions $\{C^{(0)}_{L_j}\}$ of the set of equations

$$\frac{\partial F}{\partial C_{L_j}}=0, \quad L_j=0,\ldots,L. \tag{23}$$

The stable vortex states are determined by the usual criterium for a multivariable function: the matrix of second derivative (also called the Hessian matrix),

$$\left.\frac{\partial^2 F}{\partial C_{L_j}\partial C_{L_k}}\right|_{C_{L_j}=C^{(0)}_{L_j},C_{L_k}=C^{(0)}_{L_k}}, \tag{24}$$

must be positive definite. The giant vortices are also described by Eq. (22): they correspond to $C^{(0)}_{L_j}$ except for one nonzero coefficient $C^{(0)}_{L_j=L}$. This allows us to check the stability of a giant vortex with respect to transitions into a multivortex state.

Let us consider states which are built up by only two components in Eq. (22). This restricts our analysis quantitatively but, nevertheless, will give the correct qualitative behavior and facilitates the physical insight into the problem. The free energy of a two-component state is

$$F=C^4_{L_1}A_{L_1}+C^4_{L_2}A_{L_2}+4C^2_{L_1}C^2_{L_2}A_{L_1,L_2}+2\Lambda_{L_1}C^2_{L_1}B_{L_1}+2\Lambda_{L_2}C^2_{L_2}B_{L_2}, \tag{25}$$

where

$$A_{L_i}=\frac{2\pi d}{V}\int_0^R \rho d\rho\, f^4_{L_i}(\rho),$$

$$A_{L_1,L_2}=\frac{2\pi d}{V}\int_0^R \rho d\rho\, f^2_{L_1}(\rho) f^2_{L_2}(\rho),$$

$$B_{L_i}=\frac{2\pi d}{V}\int_0^R \rho d\rho\, f^2_{L_i}(\rho),$$

and Λ_{L_i} is determined by Eq. (19). Although, in general C_{L_i} is a complex number, for our two-component state C_{L_i} is a real number. Minimization of Eq. (25) with respect to C_{L_1} and C_{L_2} gives the possible equilibrium states:

(i) the normal state,

$$C^{(0)}_{L_1}=C^{(0)}_{L_2}=0; \tag{26}$$

(ii) the giant vortex states,

$$C^{(0)}_{L_1}=0, \quad C^{(0)}_{L_2}=(-\Lambda_{L_2}B_{L_2}/A_{L_2})^{1/2},$$

$$C^{(0)}_{L_1}=(-\Lambda_{L_1}B_{L_1}/A_{L_1})^{1/2}, \quad C^{(0)}_{L_2}=0; \tag{27}$$

(iii) the multivortex states

$$C^{(0)}_{L_1}=\pm\left(\frac{-\Lambda_{L_1}A_{L_2}B_{L_1}+2\Lambda_{L_2}A_{L_1,L_2}B_{L_2}}{A_{L_1}A_{L_2}-4A^2_{L_1,L_2}}\right)^{1/2},$$

$$C^{(0)}_{L_2}=\pm\left(\frac{-\Lambda_{L_2}A_{L_1}B_{L_2}+2\Lambda_{L_1}A_{L_1,L_2}B_{L_1}}{A_{L_1}A_{L_2}-4A^2_{L_1,L_2}}\right)^{1/2}. \tag{28}$$

The components of the matrix (24) are

$$\frac{\partial^2 F}{\partial C^2_{L_1}}=12C^2_{L_1}A_{L_1}+8C^2_{L_2}A_{L_1,L_2}+4\Lambda_{L_1}B_{L_1},$$

$$\frac{\partial^2 F}{\partial C^2_{L_2}}=12C^2_{L_2}A_{L_2}+8C^2_{L_1}A_{L_1,L_2}+4\Lambda_{L_2}B_{L_2},$$

$$\frac{\partial^2 F}{\partial C_{L_1}\partial C_{L_2}}=16C_{L_1}C_{L_2}A_{L_1,L_2}. \tag{29}$$

Substituting the solutions (26)–(28) into Eq. (25) we obtain the energies of the different equilibrium states and [from Eq. (29)] the corresponding conditions of their stability.

For the *normal state* we obtain $F=0$. Notice from Eq. (29) that for negative $\Lambda_{L_1(L_2)}$ this state is always unstable. The energies of the *giant vortex states* are

$$F_{L_i}=-\Lambda_{L_i}^2 B_{L_i}^2/A_{L_i}, \quad i=1,2. \tag{30}$$

They coincide with the F of Eq. (21). The conditions for stability are

$$\frac{\partial^2 F}{\partial C_{L_1}^2}=\frac{4}{A_{L_2}}(\Lambda_{L_1}A_{L_2}B_{L_1}-2\Lambda_{L_2}A_{L_1,L_2}B_{L_2})>0,$$

$$\frac{\partial^2 F}{\partial C_{L_2}^2}=-8\Lambda_{L_2}B_{L_2}>0, \tag{31}$$

and

$$\frac{\partial^2 F}{\partial C_{L_1}^2}=-8\Lambda_{L_1}B_{L_1}>0,$$

$$\frac{\partial^2 F}{\partial C_{L_2}^2}=\frac{4}{A_{L_1}}(\Lambda_{L_2}A_{L_1}B_{L_2}-2\Lambda_{L_1}A_{L_1,L_2}B_{L_1})>0, \tag{32}$$

for the giant vortex states with L_1 and L_2 vorticity, respectively.

The superconducting current density has only an azimuthal component and is given by

$$j_{L_i}(\rho)=-\frac{\Lambda_{L_i}B_{L_i}}{A_{L_i}}\left(\frac{L_i}{\rho}-\frac{H\rho}{2}\right)f_{L_i}^2(\rho), \quad i=1,2. \tag{33}$$

The energy of the *multivortex state* becomes

$$F_{L_1,L_2}=\frac{-\Lambda_{L_1}^2A_{L_2}B_{L_1}^2-\Lambda_{L_2}^2A_{L_1}B_{L_2}^2+4\Lambda_{L_1}\Lambda_{L_2}A_{L_1,L_2}B_{L_1}B_{L_2}}{A_{L_1}A_{L_2}-4A_{L_1,L_2}^2}, \tag{34}$$

and the corresponding conditions for its stability are

$$\frac{\partial^2 F}{\partial C_{L_1}^2}=\frac{8A_{L_1}(-\Lambda_{L_1}A_{L_2}B_{L_1}+2\Lambda_{L_2}A_{L_1,L_2}B_{L_2})}{A_{L_1}A_{L_2}-4A_{L_1,L_2}^2}>0,$$

$$\frac{\partial^2 F}{\partial C_{L_2}^2}=\frac{8A_{L_2}(-\Lambda_{L_2}A_{L_1}B_{L_2}+2\Lambda_{L_1}A_{L_1,L_2}B_{L_1})}{A_{L_1}A_{L_2}-4A_{L_1,L_2}^2}>0, \tag{35}$$

$$\frac{\partial^2 F}{\partial C_{L_1}^2}\cdot\frac{\partial^2 F}{\partial C_{L_2}^2}-\left(\frac{\partial^2 F}{\partial C_{L_1}\partial C_{L_2}}\right)^2=\frac{64(-\Lambda_{L_1}A_{L_2}B_{L_1}+2\Lambda_{L_2}A_{L_1,L_2}B_{L_2})(-\Lambda_{L_2}A_{L_1}B_{L_2}+2\Lambda_{L_1}A_{L_1,L_2}B_{L_1})}{A_{L_1}A_{L_2}-4A_{L_1,L_2}^2}>0.$$

The superconducting current density in the multivortex state is

$$j_{L_1,L_2}(\rho,\varphi)=(C_{L_1}^{(0)})^2f_{L_1}^2(\rho)\left(\frac{L_1}{\rho}-\frac{H\rho}{2}\right)+(C_{L_2}^{(0)})^2f_{L_2}^2(\rho)\left(\frac{L_2}{\rho}-\frac{H\rho}{2}\right)+C_{L_1}^{(0)}C_{L_2}^{(0)}f_{L_1}(\rho)f_{L_2}(\rho)\left(\frac{L_1+L_2}{\rho}-H\rho\right)\cos(L_2-L_1)\varphi \tag{36}$$

with $C_{L_1}^{(0)}$ and $C_{L_2}^{(0)}$ from Eq. (28).

The energies of the equilibrium vortex states are plotted in Figs. 6(a)–(c) for different values of ξ/b and disk radius $R/\xi=2.0$ and in Fig. 6(d) also for a larger radius $R/\xi=3.0$. The corresponding $M(H)$ curves are shown in Figs. 7(a)–(d). The giant vortex states (solid curves) are given by their L value and the multivortex states (dashed curves) by $(L_1{:}L_2)$, i.e., the angular momentum values of which they are composed. There exist regions of magnetic field where the giant vortex states become unstable which result in free-energy curves which extend over a smaller magnetic field range than in Figs. 3(a)–(c). For example, the separated $L=9$ state of Fig. 3(b) for $\xi/b=-0.1$ is no longer stable and thus not present in Fig. 6(b). Notice, that the ringlike vortex ($L=0, n=1$) for $\xi/b=-0.2$ became unstable too.

In case of $\xi/b=0$ a disk with radius $R/\xi=2.0$ does not exhibit any *stable* multivortex states. The multivortex states are unstable and correspond to the saddle points of the $F(C_{L_1},C_{L_2})$ function. Their energies (which are shown by dotted curves in Fig. 6) are slightly larger than the energies of the corresponding giant vortices. The saddle points are the lowest energy barriers which separate the different stable giant vortex states. At the magnetic field where the giant vortex loses stability its energy becomes equal to the energy of the saddle-point state. For the considered radius the states with small $L=0,1,2$ transit through a first-order transition to states having a different L value. For example, for $\xi/b=0$

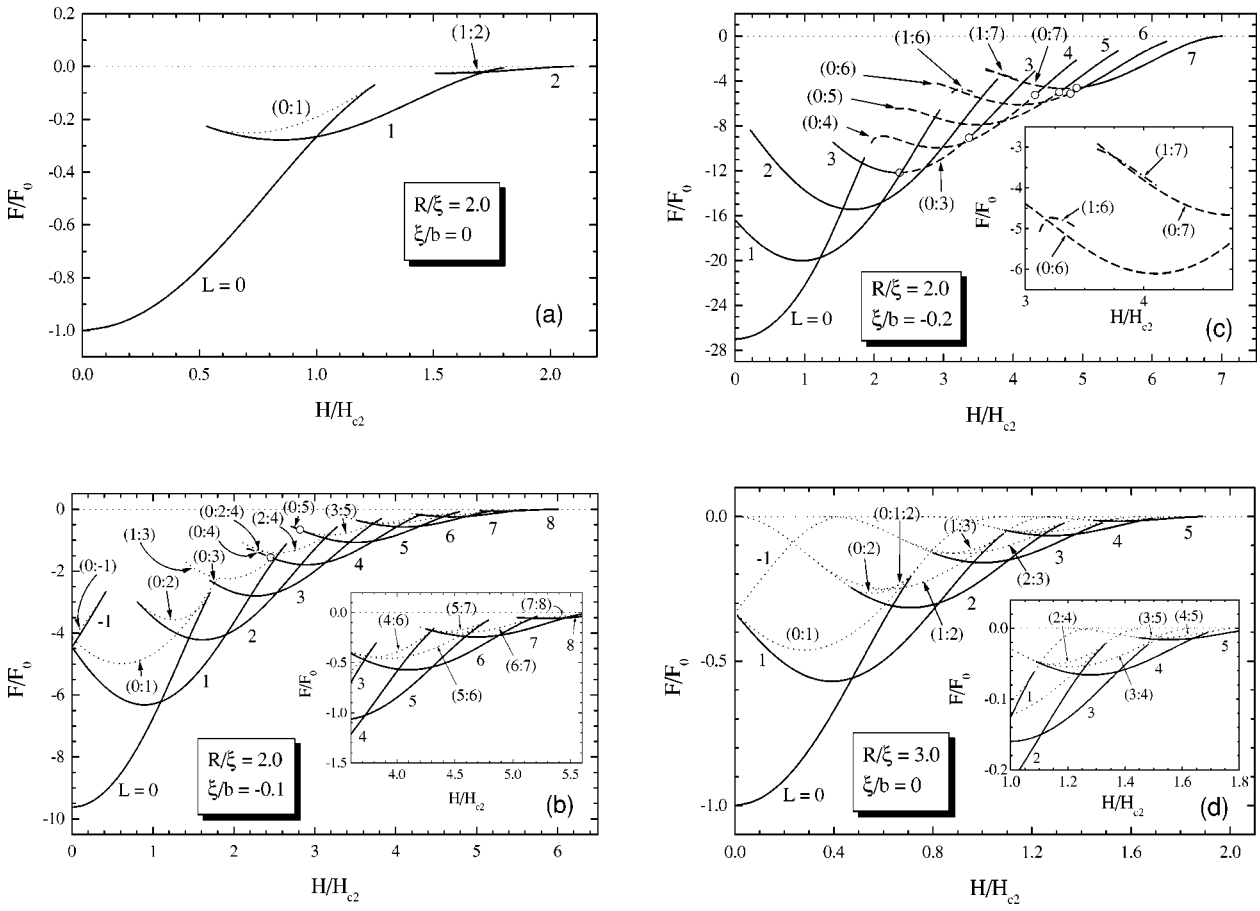

FIG. 6. The free energy of the ground state and some of the metastable and saddle-point states as a function of the external magnetic field for: (a) $\xi/b=0, R/\xi=2.0$; (b) $\xi/b=-0.1, R/\xi=2.0$, (c) $\xi/b=-0.2, R/\xi=2.0$, and (d) $\xi/b=0, R/\xi=3.0$. The solid and dashed curves are the stable giant vortex and multivortex states, respectively. The saddle-point states are shown in (a), (b), and (d) by the dotted curves where in (b) only those saddle-point states are shown which lead to transitions between different L states.

the energies of the $L=0$ and $L=1$ states are equal at $H=H_{c2}$, while the $0\rightarrow1$ transition takes place at $H=1.25H_{c2}$ when increasing the field.

With increasing $|\xi/b|$ the multivortices become more stable and they can even become the minimum of the $F(C_{L_1},C_{L_2})$ function. For example, in Fig. 8 the contour plots of this function for two different multivortex states in a disk with radius $R/\xi=2.0$ and $\xi/b=-0.2$ are shown. At $H=1.4H_{c2}$ the $(0:2)$ state is unstable [cross in Fig. 8(a)] whereas the Meissner state and the $L=2$ giant vortex state correspond to minima of the energy (the $L=2$ state is the local minimum and the $L=0$ state is the global one). At $H=2.3H_{c2}$ the $(0:4)$ multivortex state corresponds to the minimum of energy [solid dot in Fig. 8(b)] and both the Meissner state and the $L=4$ giant vortex state became the saddle points of the $F(C_{L_1},C_{L_2})$ function.

For $\xi/b=-0.1$ multivortices exist only as metastable states. The transitions between the giant and multivortex with the *same* vorticity are of second order (they are indicated by open circles in Figs. 6 and 7). With increasing magnetic field the single vortices in the multivortex state become broader, they move towards each other and merge in a continuous way into a giant vortex.[6] For $\xi/b=-0.2$ [Fig. 6(c)] the multivortices exist in the ground state for $3\leqslant L\leqslant6$. At $H=4.825H_{c2}$ this multivortex ground state becomes the giant vortex one and for $L\geqslant7$ only giant vortex states are found as ground state.

With increasing $|\xi/b|$ the phase transitions between states with different L values become more complicated and transitions with $\Delta L>1$ are possible. For example, for a disk with $\xi/b=-0.1$, $R/\xi=2.0$ [see Fig. 6(b)] the barrier between the $L=0$ and $L=2$ states has the lowest value. In Fig. 9 the contourplot of the $|\psi|^2$ distribution for the $(0:2)$ saddle point is shown for different magnetic fields. With increasing magnetic field we clearly see that two vortices move away from the center towards the edge of the sample. It allows us to interpret the transition between $L=0$ and $L=2$ states with increasing field as the simultaneous penetration of two vortices into the disk. From Fig. 6(b) we find that in this disk with increasing field the following transitions occur: $0\rightarrow2\rightarrow4\rightarrow6\rightarrow7\rightarrow8\rightarrow$ ''*normal state*'' while with decreasing field we have ''*normal state*'' $\rightarrow8\rightarrow7\rightarrow5\rightarrow(0:5)\rightarrow3\rightarrow0$. These transitions are shown in Fig. 7(b) by the arrows. In the present approach we find that penetration (or expulsion) of more than one vortex into (from) the disk is possible. A similar situation is possible for $\xi/b=0$ when the radius of the disk is sufficiently large. For example, for a disk with $R/\xi=3.0$ [Fig. 6(d)] we obtain the transitions: $0\rightarrow2\rightarrow3\rightarrow4\rightarrow5\rightarrow$ ''*normal state*'' with increasing magnetic field, and ''*normal state*'' $\rightarrow5\rightarrow4\rightarrow2\rightarrow0$ with decreasing magnetic field [see also the corresponding arrows in Fig. 7(d)].

This picture of many vortex penetration (or expulsion) differs from Ref. 29 where it was claimed that the barriers

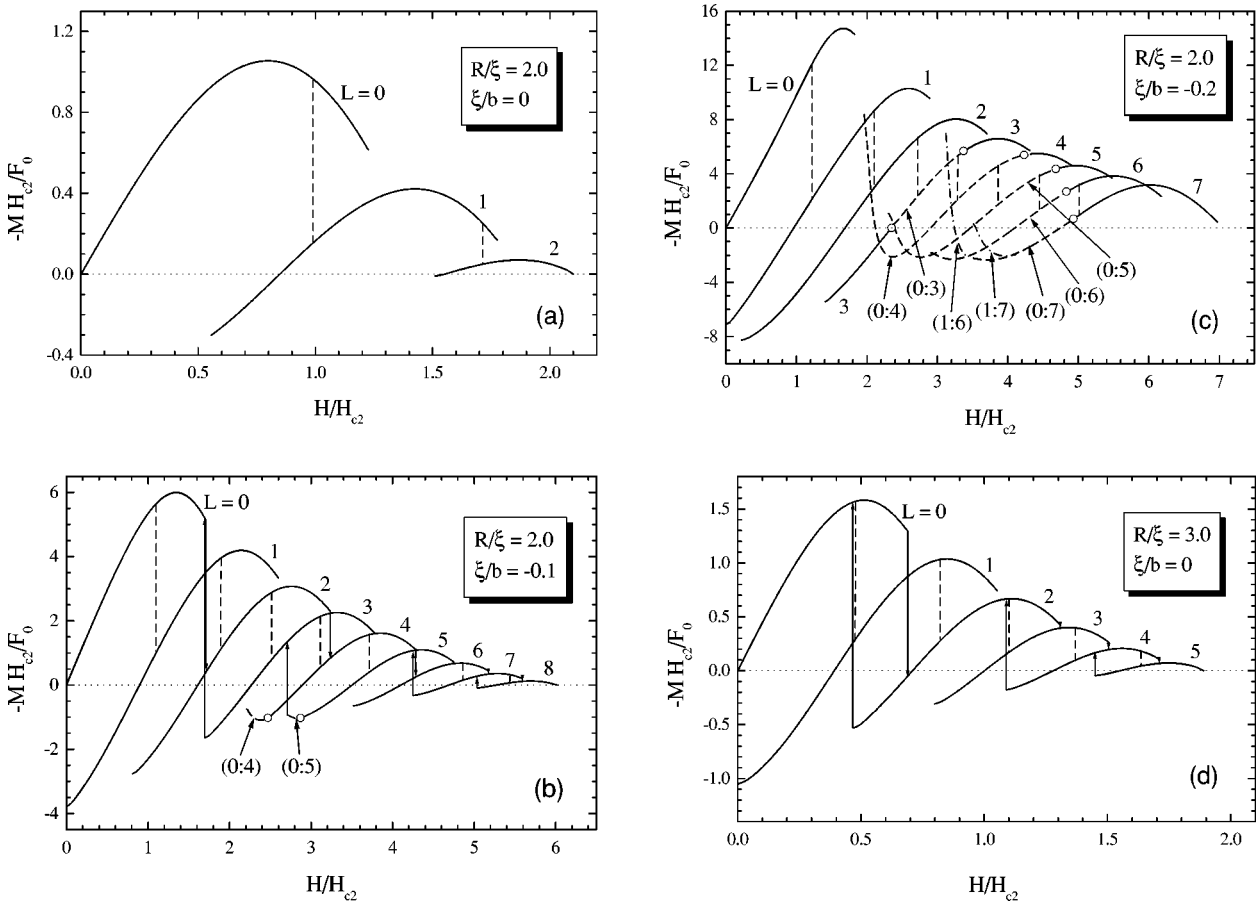

FIG. 7. The magnetic-field dependence of the disk magnetization for the stable states corresponding to the states of Fig. 6. The vertical dotted lines give the ground-state transition fields. Solid (dashed) curves correspond to the giant (multi-)vortex states.

between the L and $L\pm1$ states have the lowest value. We found that the $L\rightarrow L\pm1$ transitions take place in disks for a small maximum value of vorticity or at magnetic fields close to the ''superconducting–normal-state'' transition point. Between these two limiting regimes $L\rightarrow L\pm N$ transitions are possible with $N>1$. Our results are also in agreement with Ref. 30 where it was found numerically that several vortices can enter at once for disks with sufficiently large radius.

In Fig. 6(c) we notice that for $L=3$ vorticity there is a re-entrant (''*giant → multi → giant*'') transition. At the magnetic field $H=2.37H_{c2}$ the giant vortex separates into single vortices and at the field $H=3.36H_{c2}$ becomes a giant vortex state again. This remarkable phenomenon is illustrated in Fig. 10 where we show a contour plot of the $|\psi|^2$ distribution for this multivortex state for different magnetic field values. For $L\geqslant6$ two kinds of stable multivortex configurations[30] are possible: (i) single vortices on a single ring, and (ii) a ring structure with one vortex situated in the center of the disk. The energy of such states for $L=6,7$ vor-

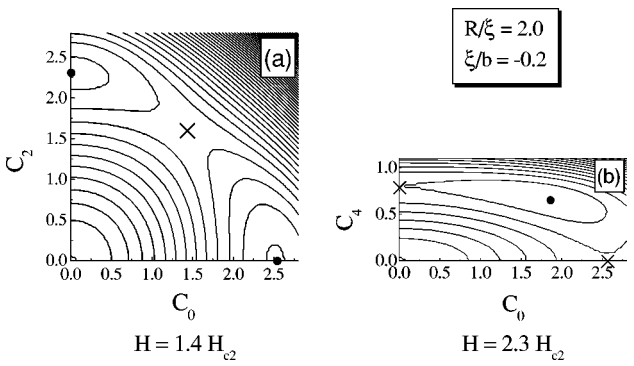

FIG. 8. Contour plot of the $F(C_{L_1},C_{L_2})$ function for two different magnetic-field values. The black circles correspond to the minima and the saddle points are shown by crosses. In (a) the Meissner state (with $L=0$) has the lowest energy while in (b) the $(0:4)$ multivortex state is the ground state.

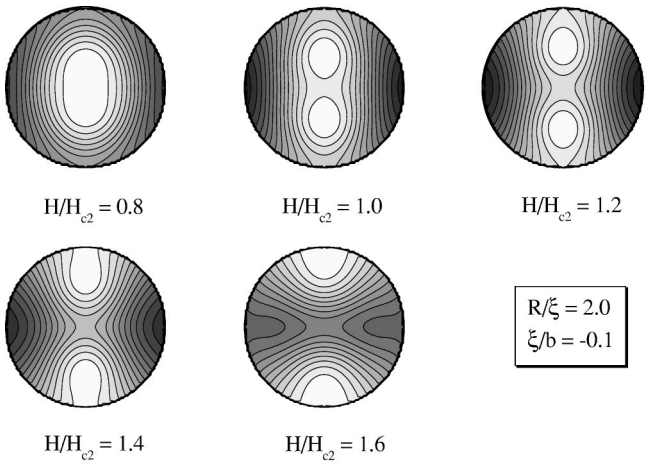

FIG. 9. Contour plot of the superconducting density for the $(0:2)$ saddle-point state [see Fig. 6(c)] for different magnetic fields.

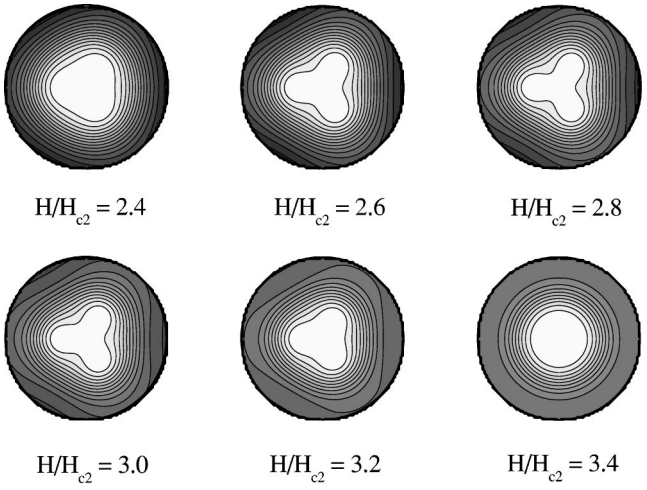

FIG. 10. Contour plot of the superconducting density for the (0:3) stable multivortex state [see Fig. 6(c)] for different magnetic fields.

ticity is plotted in the inset of Fig. 6(c) and the corresponding contour plots of the density distribution $|\psi|^2$ are given in Fig. 11 at the magnetic field $H=3.3H_{c2}$ for $L=6$ vorticity and at the field $H=3.6H_{c2}$ for $L=7$ vorticity. The difference in vortex configurations is clearly visible from these contour plots.

It should be noted that in order to find the region of stability of the multivortex states in the above analysis we had to take the order parameter as a linear combination of *three* components in Eq. (22) and to minimize the free energy with respect to three variational parameters C_{L_i}. The giant and multivortex states considered before correspond to the extremum points of the $F(C_{L_1},C_{L_2},C_{L_3})$ function. The contour plots of the $F(C_{L_i},C_{L_j})$ function for different $(L_i:L_j)$ states can be represented as a projection of the $F(C_{L_1},C_{L_2},C_{L_3})$ function on the corresponding (C_{L_i},C_{L_j}) plane. Now the Hessian matrix of $F(C_{L_1},C_{L_2},C_{L_3})$ is 3×3 dimensional and has *three* eigenvalues. Consequently, we can have two different kinds of saddle points: (i) the Hessian matrix has only *one* negative eigenvalue [for example, for $L=2$ the unstable state in Fig. 6(d) at the magnetic field region $0.31\leqslant H/H_{c2}\leqslant0.46$]; (ii) the Hessian matrix has *two* negative eigenvalues [for example, the (1:2) state in Fig. 6(d) at the same field region]. As a result in Figs. 6(b) and (d) there are connections between curves corresponding to two different unstable states. These unstable states differ by the number of the negative eigenvalues in the Hessian matrix. Moreover, by the same reason there are unstable $(L:L+1:L+2)$ states corresponding to barriers between the $(L:L+1)$ and $(L+1:L+2)$ unstable states [for example, in Fig. 6(d) the energy of the (0:1:2) state is shown]. Due to the presence of such states there is the possibility to realize the above $L\rightarrow L\pm2$ transitions between stable giant vortex states through the $L\rightarrow L\pm1\rightarrow L\pm2$ transition sequence via the intermediate unstable $L\pm1$ state.

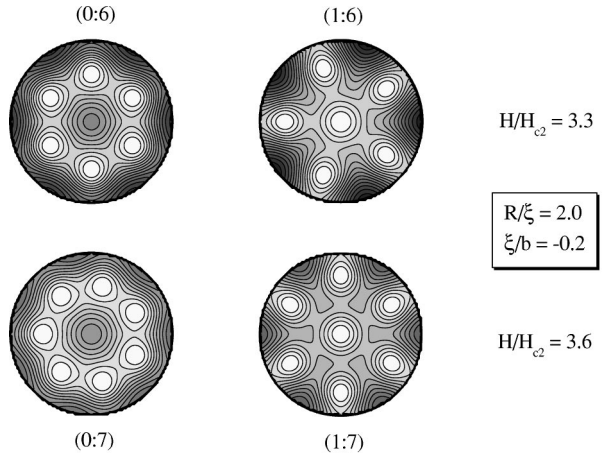

FIG. 11. Contour plot of the superconducting density for two stable multivortex states with $L=6$ and $L=7$ vorticity [see Fig. 6(c)] for different multivortex configurations.

The above transiton in a disk with $\xi/b=-0.1$, $R/\xi=2.0$ from the (0:5) multivortex state to $L=3$ giant vortex state with decreasing magnetic field also is realized through the intermediate saddle-point state. The first step is the transition from the (0:5) stable multivortex to the (3:5) unstable state [via the (0:3:5) saddle-point one]. After that the transition to the $L=3$ state takes place which corresponds to expulsion of two vortices from the disk.

Notice that for the disk parameters which we used, an increase of the number of components in Eq. (22) does not lead to different vortex states in the ground state. In general, for larger disks more complicate configurations with a larger number of components are possible (see, for example, Refs. 7 and 8).

V. *H-T* PHASE DIAGRAM

Up to now all our calculations were done for fixed temperature T. The temperature is indirectly included in the units we used, namely, into ξ,λ,H_c,H_{c2} whose temperature dependence is as follows:

$$\xi=\xi(0)\left|1-\frac{T}{T_{c0}}\right|^{-1/2},\quad \lambda=\lambda(0)\left|1-\frac{T}{T_{c0}}\right|^{-1/2},$$

$$H_c=H_c(0)\left|1-\frac{T}{T_{c0}}\right|,\quad H_{c2}=H_{c2}(0)\left|1-\frac{T}{T_{c0}}\right|. \quad (37)$$

Now we will insert temperature explicitly and use $\xi(0)$ and $H_{c2}(0)$ as the basis for our units. Temperature will be expressed in units of the zero magnetic-field critical temperature T_{c0} for the case $\xi(0)/b=0$. After the corresponding rescaling of distances, magnetic field, and energy we can use our previous results with the only exception that for temperatures larger than T_{c0} the eigenvalues of Eq. (16) are $\Lambda=H(1+2\nu)+1-k^2$ instead of Eq. (19).

The H-T phase diagram is shown in Figs. 12 and 13 for different values of $\xi(0)/b$. The regions inside the different curves for fixed L correspond to the stability region of that L state. Notice, that the stability regions of the L states are much smaller than the regions of existence of these states following only from the solutions of Eq. (23). For example, in Fig. 12 the boundary of the region of existence of the equilibrium $L=1$ state is shown by a thin dashed line. One can see that the low-field boundary between the neighbor states differs strongly while the high-field one changes

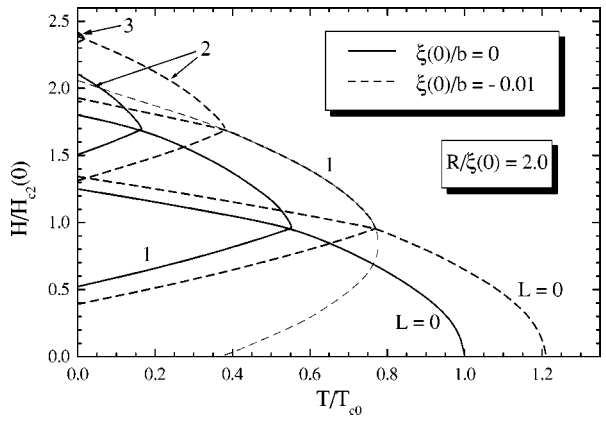

FIG. 12. The H-T phase diagram for a thin disk completely surrounded by material which enhances the surface superconductivity. For $\xi/b=-0.01$ the giant vortex states are the sole stable states. For comparison the region of existence of the equilibrium (*not necessarily stable*) $L=1$ state is shown by the thin dashed curve.

slightly. Notice that the critical temperature T_c is very sensitive to the value of $\xi(0)/b$. A change of $\xi(0)/b$ from 0 to -0.01 results in an increase of T_c from T_{c0} to $1.21T_{c0}$ (see Fig. 12). This increase is mainly due to the effect of the boundary condition on the top and bottom surface of the disk. If we include $\xi(0)/b$ only for the side surface and take $b=\infty$ at the top and bottom surfaces T_c practically does not change.

A change of $\xi(0)/b$ from 0 to -0.2 gives a significant increase of T_c from T_{c0} to $5.21T_{c0}$ (see Fig. 13). In the latter case the phase diagram becomes richer. It has regions deep inside the superconducting state where various multivortex states are stable (see inset in Fig. 13). With decreasing field the system starts as a giant vortex (GV) state, it transits to a multivortex (MV) state and than back to a giant vortex (GV) state. Within a multivortex state of $L=6$ and $L=7$ different

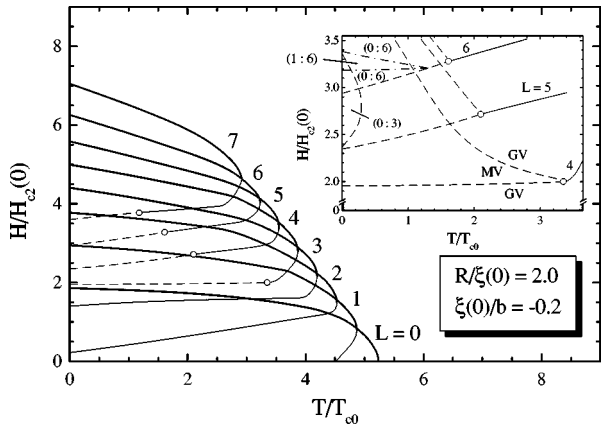

FIG. 13. The H-T phase diagram for a thin disk with both giant and multivortex states for $\xi/b=-0.2$. Only the regions of stability of states with $L\leqslant 7$ vorticity are shown. The thick solid curves are the boundaries of the stabilty regions for increasing magnetic field. Thin solid curves are the boundaries for decreasing magnetic field, where the dashed curves are those in which the state is in the multivortex state. The inset is an enlargement of the region deep inside the superconducting state. The dashed curves delimit the stability regions of the $(0{:}L)$ multivortex states. The dash-dotted curves delimit the region of the metastable $(1{:}6)$ multivortex state.

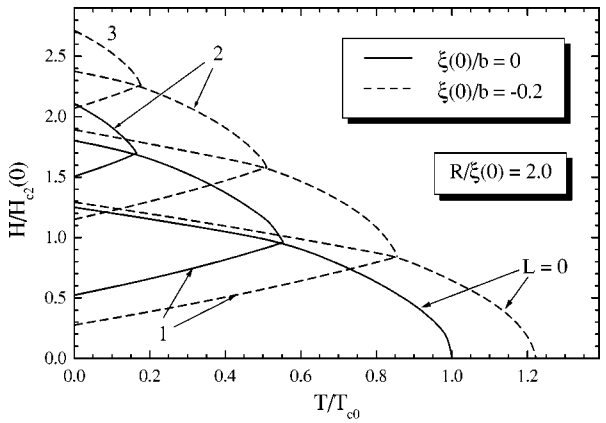

FIG. 14. The H-T phase diagram for a thin disk with enhancement of superconductivity only at the radial disk side. The regions of stability of possible states are shown.

configurations are possible. The boundaries of such states are shown by the dash-dotted curves for the case of $L=6$. For very low temperature there is also a small region where the $(0{:}3)$ multivortex state is stable. Notice also that near the ''superconductor–normal-state'' boundary only the giant vortex states exist.

Now we will investigate the influence of the superconductivity enhancement by the disk top and bottom surfaces with respect to the radial side surface contribution. The ratio of the surface area of the disk ''top-bottom'' versus the one of the radial wall is $S_{t-b}/S_{rad}=R/d\gg 1$. As a consequence the contribution from the ''top-bottom'' surface to the enhancement of superconductivity is the dominant one. To discriminate both effects we separate the BC (8) and consider two cases:

(i) the enhancement of superconductivity on the radial side boundary only. The corresponding boundary conditions are

$$\vec{n}\cdot(-i\vec{\nabla}-\vec{A})\psi|_{z=\pm d/2}=0, \quad \left.\frac{\partial\psi}{\partial\rho}\right|_{\rho=R}=-\frac{1}{b}\psi\Big|_{\rho=R}. \tag{38}$$

In this case we can make the averaging procedure on the disk thickness from the beginning and use the results of Sec. III with $k=0$.

(ii) the enhancement of superconductivity on the top-bottom surface only. The boundary conditions are

$$\vec{n}\cdot(-i\vec{\nabla}-\vec{A})\psi|_{z=\pm d/2}=\frac{i}{b}\psi\Big|_{z=\pm d/2}, \quad \left.\frac{\partial\psi}{\partial\rho}\right|_{\rho=R}=0. \tag{39}$$

Here the calculations are similar as in Sec. III but instead of Eq. (18) we have to solve the equation

$$\left(L-\frac{\Phi}{2}\right)M\left(-\nu,L+1,\frac{\Phi}{2}\right)-\frac{\nu\Phi}{L+1}M\left(-\nu+1,L+2,\frac{\Phi}{2}\right)=0. \tag{40}$$

The H-T phase diagram for $\xi(0)/b=0$ and -0.2 is shown in Fig. 14 for a disk with enhanced superconductivity only on the side walls. The corresponding H-T diagram for the boundary conditions of Eq. (39) is practically the same as

the one with the boundary conditions of Eq. (4) (see Fig. 13) which was already discussed in detail. Notice that the effect of the $\xi/b \neq 0$ boundary condition on our result is indeed predominantly a result of the disk top and bottom surfaces. The enhancement of superconductivity on the disk radial side boundary influences the results to a much lesser extent as compared to the $\xi/b=0$ results. Nevertheless, this small effect promotes the penetration of a larger number of vortices at magnetic fields close to the nucleation field for the case of large $-\xi/b$. For example, when we compare in Fig. 5 the two magnetization curves for a disk with $\xi/b=-0.2$ one sees that enhancement of superconductivity on the side wall of the disk increases the maximum value of the vorticity from $L=14$ to $L=16$.

VI. CONCLUSIONS

We studied theoretically how surface enhancement of superconductivity influences the structure of the vortex state in a thin mesoscopic disk. We found that both giant vortex states and multivortex states can exist in such disks if they are sufficiently large. Numerous phase transitions are found, both first order (between states with different angular momentum values) and second order (between the giant and multivortex states with the same angular momentum). Both the giant vortex states and the multivortex states can occur as metastable states. Surface enhancement of superconductivity is found to stabilize the multivortex state as the ground state (i.e., with minimal energy). We obtained the H-T phase diagram and found that surface enhancement significantly increases the region of existence of the superconducting state (both the critical temperature and the nucleation field). The main contribution for this surface enhancement is due to the boundary conditions at the disk top and bottom surfaces. The saddle points between the different vortex states were calculated which gives us the energy barrier for flux entrance and flux expulsion. For intermediate magnetic fields we found situations in which more than one flux can enter or exit at the same time.

Finally, it must be noted that our results are only valid in the limit of very thin disks. It allowed us to separate the two GL equations because of the fact that the magnetic field may be taken uniform inside the disk. Notice also that in the limit $\kappa \gg 1$ [see Eq. (7)] the same separation of equations is possible. Therefore our results can also be applied to describe vortex structures in extreme type-II superconducting disk-shaped samples.

ACKNOWLEDGMENTS

This work was supported by the Flemish Science Foundation (FWO-Vl) and the Belgian Inter-University Attraction Poles (IUAP-Vl). One of us (S.V.Y.) is supported by a funding from DWTC (Belgium) to promote the S & T collaboration with Central and Eastern Europe. Stimulating discussions with J. Indekeu, E. Montevecchi, V. Schweigert, J. Palacios, and B. Baelus are gratefully acknowledged.

*Permanent address: Donetsk Physical & Technical Institute, National Academy of Sciences of Ukraine, Donetsk 83114, Ukraine.
†Electronic address: peeters@uia.ua.ac.be

[1] O. Buisson, P. Gandit, R. Rammel, Y.Y. Wang, and B. Pannetier, Phys. Lett. A **150**, 36 (1990).
[2] A.K. Geim, I.V. Grigorieva, S.V. Dubonos, J.G.S. Lok, J.C. Maan, A.E. Filippov, and F.M. Peeters, Nature (London) **390**, 259 (1997).
[3] P.S. Deo, V.A. Schweigert, F.M. Peeters, and A.K. Geim, Phys. Rev. Lett. **79**, 4653 (1997).
[4] R. Benoist and W. Zwerger, Z. Phys. B: Condens. Matter **103**, 377 (1997).
[5] V.A. Schweigert and F.M. Peeters, Phys. Rev. B **57**, 13 817 (1998).
[6] V.A. Schweigert, F.M. Peeters, and P.S. Deo, Phys. Rev. Lett. **81**, 2783 (1998).
[7] J.J. Palacios, Physica B **256-258**, 610 (1998).
[8] J.J. Palacios, Phys. Rev. B **58**, R5948 (1998).
[9] E. Akkermans and K. Mallick, J. Phys. A **32**, 7133 (1999).
[10] P.S. Deo, F.M. Peeters, and V.A. Schweigert, Superlattices Microstruct. **25**, 1195 (1999).
[11] G.M. Braverman, S.A. Gredeskul, and Y. Avishai, Phys. Rev. B **59**, 12 039 (1999).
[12] V.V. Moshchalkov, L. Gielen, C. Strunk, R. Jonckheere, X. Qiu, C. van Haesendonck, and Y. Bruynseraede, Nature (London) **373**, 319 (1995).
[13] A. Houghton and F.B. McLean, Phys. Lett. **19**, 172 (1965); A.P. van Gelder, Phys. Rev. Lett. **20**, 1435 (1968).
[14] V.A. Schweigert and F.M. Peeters, Phys. Rev. B **60**, 3084 (1999).
[15] F. Brosens, J.T. Devreese, V.M. Fomin, and V.V. Moshchalkov, Solid State Commun. **111**, 565 (1999); S.N. Klimin, V.M. Fomin, J.T. Devreese, and V.V. Moshchalkov, *ibid.* **111**, 589 (1999).
[16] P.G. de Gennes, *Superconductivity of Metals and Alloys* (Addison-Wesley, New York, 1994).
[17] S. Takács, Czech. J. Phys., Sect. B **19**, 1366 (1969).
[18] H.J. Fink and W.C.H. Joiner, Phys. Rev. Lett. **23**, 120 (1969).
[19] I.N. Khlyustikov and A.I. Buzdin, Adv. Phys. **36**, 271 (1987).
[20] J.O. Indekeu, F. Clarisse, and E. Montevecchi (unpublished).
[21] J.O. Indekeu and J.M.J. van Leeuwen, Phys. Rev. Lett. **75**, 1618 (1995); Physica C **251**, 290 (1995).
[22] R. Blossey and J.O. Indekeu, Phys. Rev. B **53**, 8599 (1996).
[23] V.A. Schweigert and F.M. Peeters, Phys. Rev. Lett. **83**, 2409 (1999).
[24] R.O. Zaitsev, Zh. Éksp. Teor. Fiz. **48**, 1759 (1965) [Sov. Phys. JETP **21**, 1178 (1965)].
[25] A. Bezryadin, Yu.N. Ovchinnikov, and B. Pannetier, Phys. Rev. B **53**, 8553 (1996).
[26] V.V. Moshchalkov, X.G. Qiu, and V. Bruyndoncx, Phys. Rev. B **55**, 11 793 (1997).
[27] *Handbook of Mathematical Functions*, edited by M. Abramovitz and I. Stegun (Dover Publications, New York, 1970), p. 504.
[28] J. Govaerts, G. Stenuit, D. Bertrand, and O. van der Aa, Phys. Lett. A **267**, 56 (2000).
[29] J.J. Palacios, Phys. Rev. Lett. **84**, 1796 (2000).
[30] V.A. Schweigert and F.M. Peeters, Physica C **332**, 266 (2000).